Research Square

Preprints are preliminary reports that have not undergone peer review.
They should not be considered conclusive, used to inform clinical practice,
or referenced by the media as validated information.

A three-level closed-loop control method of double eccentric ring mechanism of the rotary steerable system based on energy

Wangliang Xiang
Yangtze University
Lei Shi
shilei0909@163.com

Yangtze University
Shengqian Ruan
Yangtze University
Xiangjin Lin
Yangtze University
Jiafan Zhang
Yangtze University
Xinjian Cao
Huaibei Institute of Technology

Research Article

Keywords: double eccentric ring mechanism, energy constraint, three-level closed-loop control, rotary steerable system, GD32 microcontroller

Posted Date: November 11th, 2026

DOI: https://doi.org/10.21203/rs.3.rs-11436615/v1

License: This work is licensed under a Creative Commons Attribution 4.0 International License.
Read Full License

Additional Declarations: No competing interests reported.

A three-level closed-loop control method of double eccentric ring mechanism of the rotary steerable system based on energy constraint

Wangliang Xiang[1], Lei Shi[1],* Shengqian Ruan[1], Xiangjin Lin[1], Jiafan Zhang[1], Xinjian Cao[2]

[1] School of Mechanical Engineering, Yangtze University, Jingzhou 434023, China

[2] Huaibei Institute of Technology, Huaibei 235000, China

* Corresponding author. E-mail: shilei0909@163.com

Lei Shi：Ph.D., Associate Professor

Wangliang Xiang / Shengqian Ruan / Xiangjin Lin / Jiafan Zhang：MSc

Xinjian Cao：MSc, Instructor

Abstract: Aiming at the problem that it is difficult to balance the non-overshoot positioning and fast response under the unidirectional rotation constraint of the double eccentric ring mechanism of the rotary steerable system, this paper proposes a three-level closed-loop control method of speed planning based on the principle of energy constraint. This method constructs a position-speed-voltage hierarchical control architecture. The position loop calculates the maximum safe speed under the constraint of residual angle in real time according to energy conservation, so as to ensure that the system brakes at the target position after the driving force is removed, and the overshoot is eliminated from the root. The speed loop uses back electromotive force feedforward mapping to avoid integral saturation. The voltage loop performs saturation limiting and dead zone management. The simulation results show that the positioning error of this method is less than 0.0381° in the whole angle range from 1° to 360°, and the convergence time of small angle condition is about 6 times shorter than that of cascade PID, and the parameters do not need to be re-tuned with the change of target angle. The experimental prototype with GD32 microcontroller as the core has a positioning error of less than 0.8° and a continuous operating temperature of less than 44° C under 10 typical working conditions.

Keyword: double eccentric ring mechanism; energy constraint; three-level closed-loop control; rotary steerable system; GD32 microcontroller

1 Introduction

The exploration and development of global oil and gas resources is continuously expanding to deep and complex formations. This trend makes extended reach wells, horizontal wells, branch wells and other complex structural wells become an indispensable technical choice for the efficient development of unconventional oil and gas reservoirs. Rotary Steerable System (RSS), as the core equipment for precise control of wellbore trajectory, can adjust the bit direction in real time during the continuous rotation of drill string, and realize the closed-loop dynamic control of wellbore trajectory[1]. With the continuous development of unconventional oil and gas resources, the application of RSS in complex structure wells is becoming more and more extensive, which has become a key technical means to determine drilling efficiency and wellbore quality[2]. At the same time, in order to improve the efficiency of tool drilling and reduce the error interference caused by manual operation, RSS is accelerating in the direction of downhole closed-loop automation and intelligence.

Scholars at home and abroad have carried out a lot of research on the guidance control of rotary steering

tools. The evolution of control methods can be roughly divided into three levels.

At the level of classical control methods, PID control and its improved form are widely used because of its simple structure and convenient engineering implementation. Abdulgalil et al.[3] designed a PID controller based on the sliding surface function to deal with the nonlinear problems caused by uncertainty in the drilling system, which effectively reduced the bit angular velocity error. The measurement and control system of stabilized platform rotary steering tool adopts double closed-loop PID controller to realize torque loop control, which can automatically maintain or adjust the tool face angle[4]. Li et al. [5] proposed a robust control method of tool face angle based on adaptive backstepping control for the stable platform of full rotary steering drilling tool. The stability of the system was proved by Lyapunov function. On this basis, Li et al. [6] further proposed a backstepping sliding mode control strategy based on nonlinear disturbance observer to deal with the disturbance and uncertainty in the tool face angle control of the stabilized platform. In terms of push-type RSS, the static push-type system uses three hydraulic modules to realize the change of the magnitude and direction of the push force acting on the wellbore. Researchers have designed and implemented the vector force closed-loop control[7].

At the level of intelligent control methods, with the rapid development of artificial intelligence technology, intelligent control strategies have gradually been introduced into the rotary steering system. Gao et al. [8] proposed an adaptive fixed-time fault-tolerant tracking control method for the rotary steering drilling tool system, and used Markov jump system to describe the parameter changes caused by environmental changes. Zhang et al. [9] proposed a deep deterministic policy gradient method based on extended state observer (DDPG_ESO) to solve the problem of accuracy and robustness in attitude control of stable platform. The researchers also proposed a BP-Fuzzy downhole closed-loop control method based on the combination of back propagation neural network and fuzzy control. The simulation results show that the method is superior to traditional PID and fuzzy control in terms of response speed, overshoot, steady-state error and anti-disturbance ability[10]. Huo et al. [11]used integral sliding mode controller to estimate uncertain disturbance to improve the calculation accuracy and anti-interference of the control system for the modeling of the friction torque of the disc valve of the rotary steering drilling tool.

In the research of the specific structure of the double eccentric ring guiding mechanism, some scholars have carried out the exploration of related control methods. Gan et al. **Error! Reference source not found.** designed a sliding mode controller based on low-pass filter to solve the chattering problem of control input signal in the control system of double eccentric ring pointing rotary steering drilling tool, which can effectively eliminate the jitter of output signal. Zhang et al. **Error! Reference source not found.** simplified the model and analyzed the dynamics of the double eccentric ring bias mechanism, and designed a double-loop integral sliding mode controller. In the control of double eccentric ring motor, Cao**Error! Reference source not found.** adopts fuzzy PID control strategy, and realizes the cooperative control of inner and outer eccentric rings through cross coupling.

Although the above research has made significant progress in the control of rotary steering system, most of the current control methods still face the following shortcomings. First, the parameter tuning of traditional PID and intelligent PID control methods is highly dependent on specific working conditions. When the target angle changes, the parameters need to be readjusted, and the universality within the full stroke range is lacking. Secondly, the existing research rarely designs the control method from the physical constraints of the one-way rotation of the double eccentric ring mechanism. Most of them passively avoid overshoot through conservative parameter tuning, and it is difficult to achieve the optimal balance between no overshoot and rapidity. Thirdly, the research on model-driven control of double eccentric ring mechanism is not sufficient, and the deep

adaptation of control logic and physical characteristics of the system needs to be strengthened.

In view of the above problems, this paper takes the static offset pointing double eccentric ring mechanism as the research object, and proposes a three-level closed-loop control method based on energy-constrained speed planning. This method constructs a position-speed-voltage three-level hierarchical closed-loop control architecture, the position loop is based on the principle of energy conservation, and the maximum safe speed is calculated in real time according to the residual angle. It can ensure that the system can brake at the target position after removing the driving force from the mechanism, and naturally has no overshoot characteristics and is independent of the target angle. The speed loop adopts the back electromotive force feedforward mapping to avoid the problems of integral saturation and phase lag. The voltage loop handles the actuator saturation limiting and starting dead zone to ensure the safe and reliable operation of the hardware system. In order to verify the feasibility of the method, this paper builds an experimental prototype of the double eccentric ring steering mechanism with GD32 microcontroller as the core. Through the simulation comparison and physical experiment of multiple sets of target angle conditions, the advantages of the proposed method in positioning accuracy, response speed and anti-disturbance ability are systematically verified, which provides technical support for the engineering application of rotary steering tools.

The remainder of this paper is organized as follows. Section 2 describes the control challenges of the double-eccentric-ring mechanism for rotary steerable tools. Section 3 establishes the mathematical model of the brushed DC-motor controlled plant. Section 4 elaborates the design procedure of the three-level closed-loop controller based on energy constraint. Simulation comparisons are conducted to demonstrate the superiority of the proposed strategy. Section 5 presents the hardware prototype and experimental results. Discussion and main findings are given in Section 6, followed by conclusions and future work in Section 7.

2 Rotary steering tool control problem

2.1 Double eccentric ring mechanism

In this paper, the static offset pointing double eccentric ring mechanism is used as the steering execution unit. By changing the relative rotation angle of the inner and outer eccentric rings, the size and direction of the offset vector are synthesized, and then the bit pointing is continuously adjusted to achieve wellbore trajectory control. The eccentric ring control mechanism framework of rotary steering drilling tool is shown in Fig. 1. It is mainly composed of inner eccentric ring drive motor, outer eccentric ring drive motor, inner eccentric ring, outer eccentric ring, ratchet bearing, gear pair and position detection element. The output end of the motor shaft is connected to other parts through the ratchet bearing. The inner eccentric ring is directly driven by the inner eccentric ring drive motor, and the outer eccentric ring is connected to the outer eccentric ring drive motor through the gear pair. The magnetic components are evenly arranged on the surface of the eccentric ring, and the angle position detection is realized with the Hall sensor.

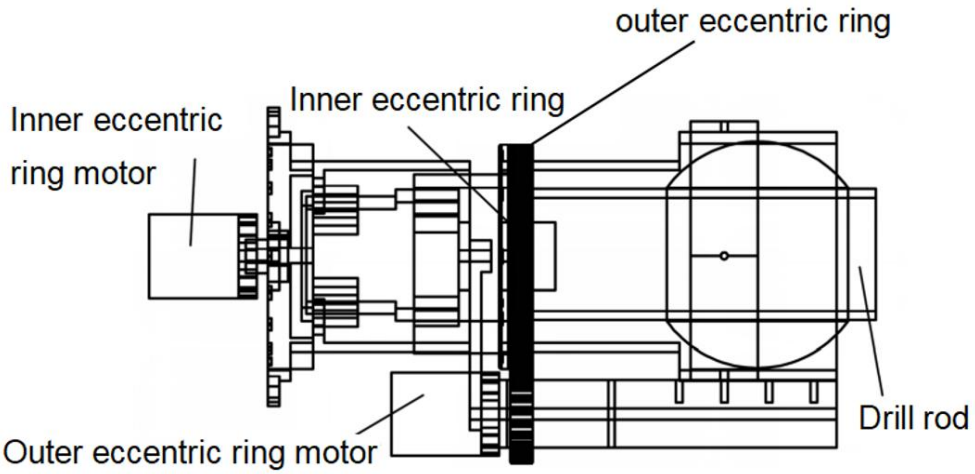


Fig. 1 Eccentric ring structure diagram

The system uses JGB37-520 brush DC motor to drive the eccentric ring rotation, and the key parameters of the motor are shown in

Tab. 1.

Tab. 1 DC motor related parameters

Parameter		Sign	Value	Dimension
model		——	JGB37-520	——
rated voltage		U_N	12	V
starting voltage		$u_{\min}$	6	V
control voltage range		u_a	$[6,\ 24]$	V
converted moment of inertia		J_m	0.05	$kg \cdot m^2$
No-load	speed	n_0	85	RPM
	current	I_0	0.1	A
Rated Load	speed	n_N	68	RPM
	power	P_N	3.6	W
	current	I_N	0.2	A
	torque	T_N	1.5	$kg \cdot cm$
Stall	torque	T_s	6	$kg \cdot cm$
	current	I_s	1.2	A

2.2 Control system architecture

The control system takes GD32 F103 RCT6 microcontroller as the core, and constructs a three-level closed-loop control architecture of position, speed and voltage. The whole system is divided into three parts: main control layer, drive execution layer and sensor feedback layer. The overall architecture of the system is shown in Fig. 2 The main control layer receives the angle control instructions issued by the host computer, runs the control algorithm and outputs the PWM drive signal ; the drive execution layer drives the eccentric ring to

rotate and execute through the motor drive circuit; the sensing feedback layer collects the driving current and tool attitude data in real time, and feeds back to the main control unit to form a full closed-loop adjustment.

The operating frequency of the processor CPU reaches 108 MHz. In order to ensure the reliability of the data, the control time step is set to 0.001 s.

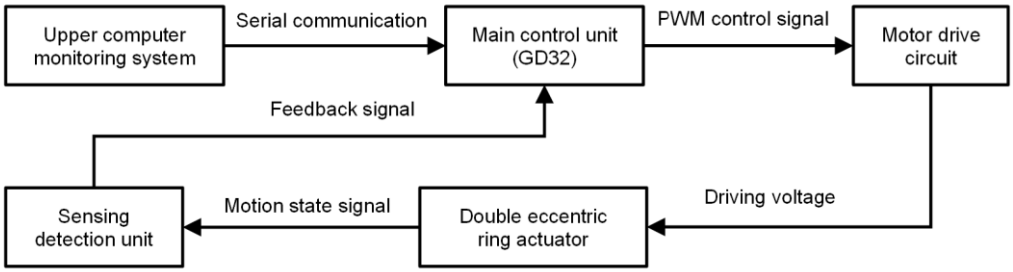


Fig. 2 Eccentric ring overall control system block diagram

2.3 Brief description of control problem

The control performance of the eccentric ring steering mechanism is the core factor that determines the trajectory adjustment accuracy and response efficiency of the rotary steering tool. Its core task is to construct a matching control algorithm model based on the position-velocity-voltage three-stage closed-loop control architecture and output the PWM drive signal in real time. The inner and outer eccentric rings are independently rotated to the target angle and docked stably. The spatial synthesis of the two-ring offset vectors obtains the drill point of the preset size and direction, and realizes the continuous and accurate control of the wellbore trajectory.

Combined with the physical limitations of the mechanism, downhole service conditions and system control objectives, the angle servo control of the eccentric ring needs to be completed under multiple constraints. The specific requirements are as follows:

(1). Armature current security constraints: limited by the power capacity of the drive circuit and the tolerance of the armature winding of the motor, the armature current of the motor needs to be limited in real time.

(2). Unidirectional rotation motion constraint: Limited by the physical characteristics of the one-way transmission of the ratchet bearing, the drive motor can only drive the eccentric ring to rotate forward ; when the ratchet structure is locked in reverse rotation, the resistance torque far exceeding the rated load of the motor will be generated, which makes the motor unable to drive the eccentric ring to rotate in reverse. Therefore, the angle adjustment can only approach the target angle through forward rotation, and does not have the ability of reverse correction. The control algorithm needs to strictly suppress the positioning overshoot to ensure that the eccentric ring docks smoothly to the target angle in one direction, and the control logic of reverse correction after overshoot should not be adopted.

(3). Angle positioning accuracy requirements: The angle control error of the inner and outer eccentric rings directly determines the synthesis accuracy of the offset vector, and ultimately affects the quality of the wellbore trajectory control.

(4). Dynamic response and stability requirements: After receiving the wellbore trajectory adjustment command, the eccentric ring needs to quickly track the target angle change and shorten the response lag time of the steering action.

(5). Three-stage closed-loop cooperative matching requirements: For the three-stage series closed-loop architecture of position, speed and voltage, it is necessary to complete the parameter matching and logic

coordination of each control loop. Under the premise of strictly satisfying the current security constraints, the positioning accuracy and response speed of the system are taken into account to achieve the optimal balance between control performance and operation safety.

3 Mathematical model of controlled object

In order to quantitatively analyze the dynamic characteristics and control effect of the control algorithm on the eccentric ring angle servo system, it is necessary to establish the mathematical model of the controlled object. The controlled object of this system is JGB37-520 brush DC motor, and its mathematical model is established by analysis method. In order to simplify the modeling process and highlight the core electromagnetic and motion laws of the system, the following assumptions are made for the model:

(1). The power devices of the system are ideal electronic components, and the resistance of the motor coil is evenly distributed,

(2). the relevant electromagnetic parameters are constant,

(3). The torsional elastic torque, viscous friction and hysteresis loss are neglected,

(4). The static friction and dynamic friction of the motor are equal.

According to the above assumptions, the mathematical model of the brush DC motor is derived, and the armature equivalent circuit is shown in Fig. 3.

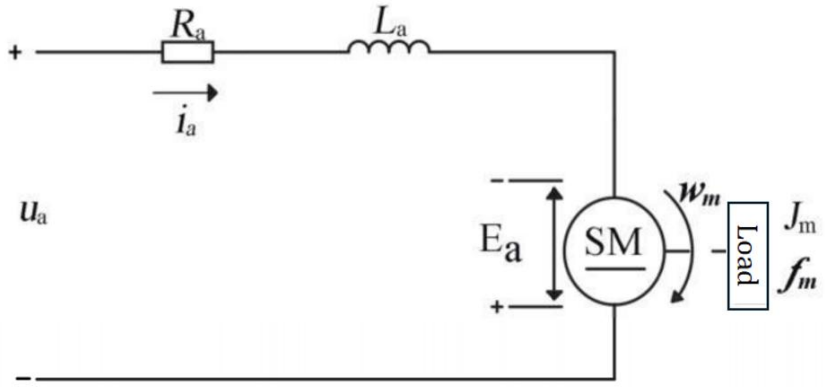


Fig. 3 DC motor armature equivalent circuit

3.1 Electromechanical coupling equation

The armature circuit voltage balance equation of brushed DC motor is:

$$u_a = E_a + R_a i_a + L_a \cdot di_a/dt \quad (1)$$

$$E_a = C_e \omega_m \quad (2)$$

Where E_a is the back electromotive force generated when the armature rotates, u_a is the voltage of the input armature, i_a is the armature current, R_a is the armature resistance, L_a is the inductance of the armature circuit, C_e is the back electromotive force coefficient, and ω_m is the speed of the motor output.

The electromagnetic torque balance equation of brushed DC motor is:

$$M_m = C_m i_a \quad (3)$$

Where M_m is the electromagnetic torque generated by the armature current, and C_m is the torque coefficient of the DC motor.

The torque balance equation on the DC motor shaft is:

$$J_m \cdot d\omega_m/dt = M_m - M_c - M_f \quad (4)$$

Where J_m is the rotational inertia of the motor and the load converted to the motor shaft, M_f is the friction torque, and M_c is the load torque.

When the motor is in the stationary phase, $\omega_m = 0$, which is static friction. The friction torque changes adaptively with the external torque. The direction is opposite to the resultant force of the electromagnetic torque and the load torque, and there is a maximum value M_s.

When $|M_{\mathrm{m}} - M_{\mathrm{c}}| \leq M_{\mathrm{s}}$, the motor remains stationary, that is, $dw_m/dt = 0, \omega_{\mathrm{m}} = 0$.

When $|M_{\mathrm{m}} - M_{\mathrm{c}}| > M_{\mathrm{s}}$, the motor breaks through the static friction, starts to rotate, and enters the dynamic friction stage.

When the motor is in operation, $\omega_{\mathrm{m}} \neq 0$, this is the dynamic friction. According to the model assumptions 3 and 4, let the dynamic friction moment and the static friction moment be equal:

$$M_f = M_s \tag{5}$$

Under steady-state no-load conditions, the motor has no external load, the speed is constant and the angular acceleration is 0, and the electromagnetic torque is all used to overcome its own friction torque. According to the torque balance relationship and the electromagnetic torque formula, the friction torque satisfies:

$$M_f = C_m i_0 \tag{6}$$

When the motor is in the stationary phase, $\omega_m = 0$, so $E_a = 0$, ignoring the transient effect of inductance. At this time, the current $i_0 = u_0/R_a$, the corresponding electromagnetic torque is:

$$M_0 = C_m \cdot u_0/R_a \tag{7}$$

Only when the electromagnetic torque is greater than the sum of the load torque $M_c(0)$ and the friction torque M_f at the initial moment, the motor will start to rotate, so the minimum starting voltage is:

$$u_{min} = R_a \cdot \left(M_c(0) + M_f\right)/C_m \tag{8}$$

Among them, the minimum starting voltage can be measured experimentally, so the relationship between the initial load torque and the starting voltage is:

$$M_c(0) = C_{\mathrm{m}} \cdot u_{\mathrm{min}}/R_{\mathrm{a}} - M_f \tag{9}$$

3.2 Structural parameter constraints

The DC motor drive circuit is shown in Fig. 4. The hardware is unipolar PWM drive, and the maximum output voltage is 24 V. Therefore, the armature voltage should meet the hard constraint:

$$0 \leq u_a \leq U_{max} \tag{10}$$

This constraint makes it impossible to output reverse voltage to generate braking torque when the motor is decelerated, and it can only be decelerated by friction torque and load torque.

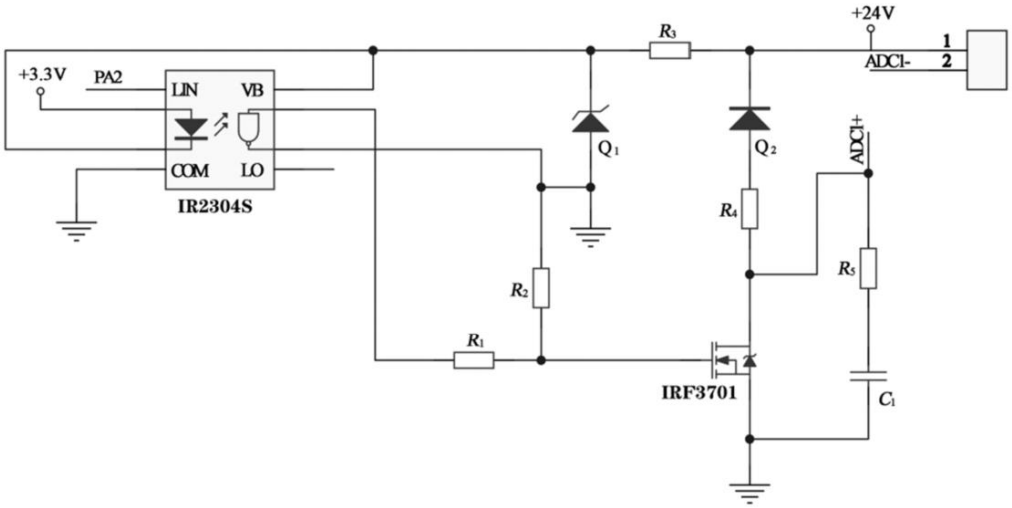


Fig. 4 Dc motor drive circuit

Limited by the physical characteristics of the one-way transmission of the ratchet bearing, the drive motor

can only drive the eccentric ring to rotate in the positive direction, so the motor speed can only rotate in the positive direction:

$$\omega_m \geq 0 \tag{11}$$

3.3 Model integration

In summary, the work of the controlled object can be divided into two stages, namely, the static stage and the running stage.

(1) Static stage

The static phase means that the motor is in a shutdown state, and the motor has no effective drive at this time. The model block diagram is as shown in the figure, input $u_a < u_{min}, \omega_m = 0$, output $\omega_m = 0$.

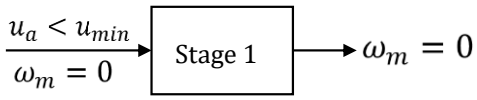


Fig. 5 Stage 1 model block diagram

(2) Running stage

The running phase indicates that the motor is working, at this time $\omega_m \neq 0$ or $u_a \geq u_{min}, \omega_m = 0$. Because the inductance L_a of the motor in the working state circuit is small, the inductance transient effect is ignored, and the differential equation of the DC motor speed ω_m and the input voltage u_a can be obtained by combining Eq. (1-4):

$$J_m \cdot d\omega_{\mathrm{m}}/dt + C_{\mathrm{m}}C_{\mathrm{e}}/R_{\mathrm{a}} \cdot \omega_m = C_{\mathrm{m}}u_a/R_{\mathrm{a}} - \left(M_c + M_f\right) \tag{12}$$

The torque term $\left(M_c + M_f\right)$ will offset part of the electromagnetic driving effect and weaken the control ability of the input voltage to the motor speed, which is the main disturbance source of the speed control system. In order to simplify the disturbance analysis and facilitate the subsequent compensation controller design, let $M_c + M_f = C_{\mathrm{m}}u_{de}/R_{\mathrm{a}}$, then the DC motor differential equation becomes:

$$J_m \cdot d\omega_{\mathrm{m}}/dt + C_{\mathrm{m}}C_{\mathrm{e}}\omega_{\mathrm{m}}/R_{\mathrm{a}} = C_{\mathrm{m}}/R_{\mathrm{a}}\left(u_{\mathrm{a}} - u_{de}\right) \tag{13}$$

Where $u_{de} = R_a \cdot \left(M_c + M_f\right)/C_m$ is the voltage disturbance.

Therefore, the dynamic transfer relationship between the effective control voltage $\left(u_{\mathrm{a}} - u_{de}\right)$ and the speed is:

$$G(s) = \Omega_m(s)/U(s) = K_m/(T_m s + 1) \tag{14}$$

$$T_m = R_a J_m/(C_m C_e) \tag{15}$$

$$K_m = 1/C_e \tag{16}$$

Where T_m is the time constant of the DC motor, and K_m is the gain of the voltage to the speed.

If the motor angle $\theta(s)$ is the output, the transfer function between the effective control voltage $\left(u_{\mathrm{a}} - u_{de}\right)$ and the output angle can be obtained by integrating the speed:

$$W(s) = \theta_m(s)/U(s) = K_m/s(T_m s + 1) \tag{17}$$

Based on the transfer function of speed and angle, the calculation model of armature real-time current can be further derived, which provides mathematical support for current closed-loop control, overcurrent protection logic and load disturbance observation. Combined with the modeling assumption that hypothesis 3 ignores the viscous friction effect, the calculation formula of the instantaneous current of the armature can be obtained from the expression (3-4):

$$i_a = \left(J_m \cdot d\omega_{\mathrm{m}}/dt + M_c\right)/C_m \tag{18}$$

In summary, $G(s)$ is the transfer function of the armature voltage U to the speed ω_{m} in stage 2, and the transfer function diagram of the DC motor system in stage 2 is shown in Fig. 6.

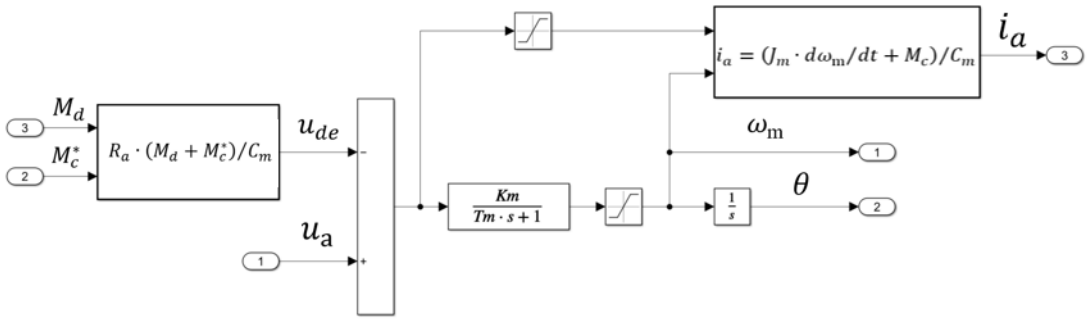


Fig. 6 Stage 2 model block diagram

3.4 Model parameter calculation

According to hypothesis 1 and 2, the parameters of the controlled object are determined. In the locked-rotor state, the armature speed is 0, the back electromotive force is 0, and the rated voltage all falls on the armature winding. Therefore, the armature resistance $R_a = U_N/I_s = 10\Omega$ can be calculated by the ratio of the rated voltage to the locked-rotor current. The torque coefficient represents the corresponding relationship between the armature current increment and the output torque increment. After deducting the loss torque corresponding to the rated current in the locked-rotor current, the output shaft equivalent torque coefficient $C_m = 0.098\,(T_s - T_N)/(I_s - I_N) = 0.4410N \cdot m/A$. The back electromotive force is obtained by subtracting the armature resistance voltage drop of the rated voltage from the rated current, and then compared with the rated output speed, the equivalent back electromotive force coefficient $C_e = (U_N - I_N \cdot R_a)/n_N = 0.1471V/RPM = 0.0245V/(°/s)$ is obtained.

According to the formulas (6), (9), (16), (17), M_f, $M_c(0)$, T_m, K_m are calculated, and the calculation results are shown in the Tab. 2.

Tab. 2 System parameter values

Parameter	Value	Dimension
M_f	0.0441	$N \cdot m$
$M_c(0)$	0.2205	$N \cdot m$
T_m	0.9423	s
K_m	47.6190	°/(s · V)

4 Controller design

In the angle control of the eccentric ring of the rotary steering drilling tool, the controlled object needs to achieve fast and non-overshoot positioning of any angle in the whole range of $[1°,\ 360°]$. Due to the limitation of mechanical structure, the motor can only rotate in one direction. The conventional PID control strategy can only perform well in fixed-point debugging, and there will be obvious overshoot or even continuous oscillation under different target angle conditions.

In this paper, a variety of control strategies such as conventional PID and fuzzy adaptive PID are tried. These methods need to change the model parameters for different target angles and do not have universality. Therefore, this chapter proposes a speed planning position control method based on the principle of energy conservation. At each sampling time, the method calculates the maximum safe speed that the system can withstand in real time according to the current residual angle, so that the driving force is removed immediately

at this speed, and the system can run out of kinetic energy just when it reaches the target position. This method naturally forms a nonlinear deceleration curve independent of the target angle, which fundamentally eliminates the possibility of overshoot.

The simulation results show that the method can achieve a stable and non-overshoot angle locking in the full range of $[1°,\ 360°]$ only by adjusting two parameters with clear physical meaning.

4.1 Control framework

The controller proposed in this paper is shown in Fig. 7. The overall framework consists of three hierarchical control loops, and the function definition of each loop is shown in

Tab. 3. Each control loop solves a problem of control, where the position loop is used to determine the limit angle that can stop at the target angle, the speed loop determines how much input voltage generates the speed, and the voltage loop is used to control the hardware constraints. Each loop has a clear physical meaning and independent tuning logic.

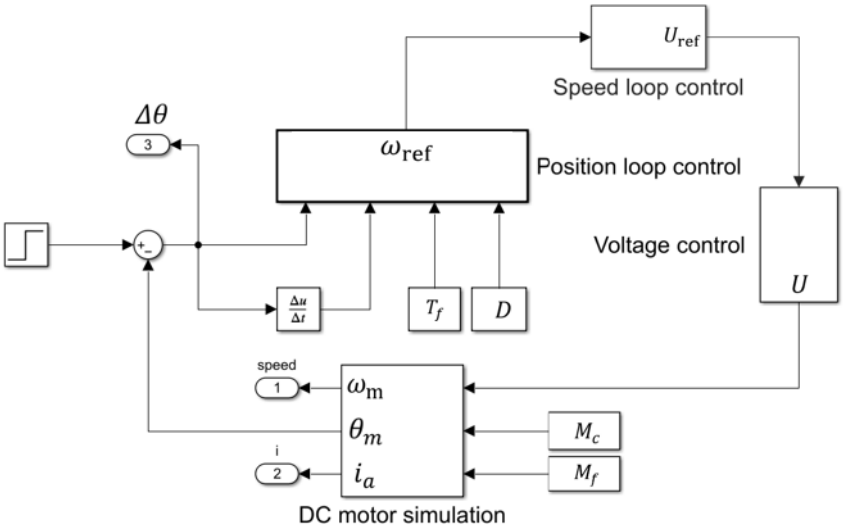


Fig. 7 The overall framework of the controller

Tab. 3 Introduction of control loop

Control layer	Functional description	Input	Output
position ring	Speed planning based on energy limitation.	$\Delta\theta,\ \dot{\Delta\theta},\ T_f, D$	target speed ω_{ref}
speed loop	Voltage mapping based on back electromotive force feedforward.	ω_{ref}	reference voltage U_{ref}
voltage control loop	Actuator saturation and dead zone management.	U_{ref}	applied voltage U

4.1.1 Position ring

The position loop is the top-level decision-making link of the control system. It does not directly output the driving voltage command, but solves the expected speed of both the response speed and the safety boundary at each sampling moment. The safety boundary refers to that when the system runs at the desired speed, once the drive is removed, it can be braked to the target position without overshoot only by means of friction damping, so as to ensure that the motor is always in the dissipation limit range of friction damping.

It is assumed that the total rotational inertia of the system converted to the output shaft of the motor is J _ m, and the total resistance torque of the system is $T_f = M_c + M_f$. When the system moves at angular velocity ω_{m}, the total rotational kinetic energy is:

$$E_{\mathrm{k}} = \frac{1}{2} J_m {\omega_{\mathrm{m}}}^2 \tag{19}$$

The dissipated work done by the frictional resistance in the residual angle $\Delta\theta$ stroke is:

$$W_f = T_f \cdot \Delta\theta \tag{20}$$

If the system is to stop at the target position without overshoot, the current kinetic energy must not exceed the maximum work dissipated by the frictional resistance in the remaining stroke:

$$\frac{1}{2} J_m {\omega_{\mathrm{m}}}^2 \leq T_f \cdot (\theta_{\mathrm{ref}} - \theta_{\mathrm{m}}) \tag{21}$$

The upper speed limit described in (21) depends only on the current residual angle. No matter what the target value is, the maximum speed allowed is the same as long as the current residual angle is the same. This property makes the speed constraint naturally independent of the target angle, which fundamentally solves the problem that the PID parameters need to be re-tuned with the change of the target angle.

From the formula (21), it can be seen that the maximum safe speed to ensure that the system can be completely stopped within the remaining angle $\Delta\theta$ is:

$$\omega_{base}(t) = \left(2T_f \cdot \Delta\theta \,/J_m\right)^{0.5} \tag{22}$$

In the actual system, T_f is uncertain with mechanical wear, temperature change and load fluctuation. When the actual resistance torque is less than the theoretical value, the system will carry excess kinetic energy during the braking process, which may lead to slight overshoot. On the contrary, when the actual resistance torque is greater than the theoretical value, the system may slow down prematurely and extend the adjustment time. For this reason, the position loop introduces a differential feedforward compensation to deal with the above uncertainty. In the braking process, if the current speed of the system is different from the defined ideal speed, the error differential $\dot{\Delta\theta}$ will reflect this deviation. When the speed is too fast, the rate of error reduction increases, $\dot{\Delta\theta}$ is negative and the absolute value is large. At this time, a negative correction term is superimposed on the speed command. When the speed is too slow, the correction term is positive. Differential feedforward compensation uses the trend of error to predict future deviations, so as to apply compensation before the deviation has not been significantly expanded. On the basis of the formula, the target angular velocity at the current moment obtained by adding differential feedforward compensation is:

$$\omega_{\mathrm{ref}}(t) = \omega_{\mathrm{base}}(t) + D \cdot \dot{\Delta\theta} \tag{23}$$

where $\dot{\Delta\theta}$ is the discrete differential of the error, and D is the differential gain coefficient.

Increasing D can enhance the anti-disturbance ability and improve the system 's insensitivity to the change of resistance moment. However, if the value is too large, it may amplify the sensor noise and cause micro-amplitude velocity fluctuation at the end.

When the residual angle is too large, the differential feedforward compensation will suppress the speed of the system and prolong the positioning time of the system. Therefore, the braking critical angle Θ_{th} of the system is defined in this paper. When $\Delta\theta > \Theta_{\mathrm{th}}$, the differential gain is forced to be set to zero, and only the basic speed command is used to ensure the positioning response ability of the system. When $\Delta\theta \leq \Theta_{\mathrm{th}}$, differential feedforward compensation is enabled to improve the end positioning accuracy and anti-interference ability. In addition, in order to avoid the numerical micro-vibration near the target point, when the position reaches the defined dead zone threshold, the velocity command is forced to zero and enter the position locking state. Based on the above analysis, the complete control law of the position loop can be expressed is:

$$\omega_{\mathrm{ref}} = \begin{cases} 0 & \Delta\theta \leq \varepsilon \\ \left(2T_f(\theta_{\mathrm{ref}} - \theta)/J_m\right)^{0.5} + D \cdot \dot{\Delta\theta} & \varepsilon < \Delta\theta \leq \Theta_{\mathrm{th}} \\ \left(2T_f(\theta_{\mathrm{ref}} - \theta)/J_m\right)^{0.5} & \Delta\theta > \Theta_{\mathrm{th}} \end{cases} \tag{24}$$

Where $\varepsilon = 0.1°$ is the dead zone threshold, and Θ_{th} is the braking critical angle.

The output ω_{ref} of the position loop is then transmitted to the speed loop, which maps it to a specific voltage command.

4.1.2 Speed loop

The traditional speed loop uses the PID controller to accumulate the speed error, which introduces the phase lag and requires a lot of gain scheduling in the full speed range. In this paper, the feedforward mapping based on the physical model of the motor is used to replace the PID error accumulation. Ignoring the inductor current, the steady-state armature voltage balance equation of the permanent magnet DC motor can be obtained from Equation (1-2):

$$U_{\text{ref}}(k) = C_e \cdot \omega_{\text{ref}}(k) + U_{\min} \tag{25}$$

Where $U_{\min}$ is the minimum starting voltage required to overcome static friction.

The mapping relationship provides instantaneous voltage command without error accumulation process, which fundamentally eliminates the problem of integral saturation, and the response phase lag is very small.

4.1.3 Voltage control loop

The primary constraint faced by the voltage loop is the physical limit of the power stage. The system is powered by a 24V DC bus. Limited by the voltage level of the drive circuit and the insulation strength of the motor, the voltage applied to the armature must not exceed $u_{\max} = 24V$.

At the same time, the drive circuit is unipolar PWM modulation, so the lower limit of voltage is 0V. When the reference voltage U_{ref} output by the speed loop exceeds the above limit, the saturation limiter will forcefully truncate it to the maximum or minimum within the allowable range. At the same time, if the reference voltage $U_{\text{ref}}(k)$ output by the speed loop is less than the minimum effective starting voltage $u_{\min}$, it is determined that the voltage instruction does not have effective driving capability and is directly forced to zero. The complete nonlinear mapping relationship of the final voltage loop is:

$$U(k) = \begin{cases} 0 & U_{\text{ref}}(k) < u_{\min} \\ U_{\text{ref}}(k) & u_{\min} \le U_{\text{ref}}(k) < u_{\max} \\ u_{\max} & u_{\max} \le U_{\text{ref}}(k) \end{cases} \tag{26}$$

4.1.4 Closed-loop dynamics

The motor drive voltage $U(k)$ output by the control method, combined with the motor work transfer function described in formula (14), can obtain the corresponding speed at the current time. The angular velocity is integrated to obtain the angle:

$$\theta(t) = \int_0^t \omega_m(\tau) d\tau \tag{27}$$

The closed-loop feedback of the angle is fed back to the input end to form a full closed-loop negative feedback control.

4.2 Control method simulation

In order to reflect the superiority of the control method proposed in this paper, the proposed method is compared with the other two methods. The three comparison methods are shown in table

Tab. 4.

Tab. 4 Details of comparison method

Method	Introduction
Method 1	The method proposed in this paper.
Method 2	PID control method is adopted.
Method 3	The control method of PID control series speed loop.

The simulation model is built by MATLAB R2025b / Simulink software. Based on the mathematical model of the controlled object, the control systems of method 2 and method 3 are constructed respectively. The simulation model is shown in Fig. 8-9.

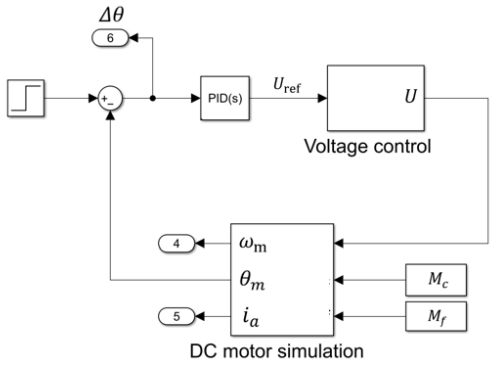


Fig. 8 Method 2 Controller overall framework

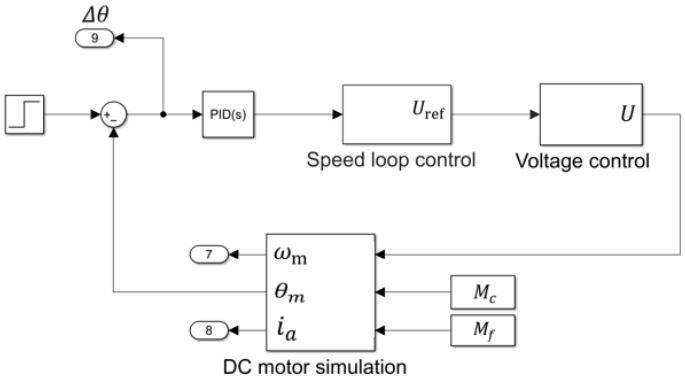


Fig. 9 Method 3 Controller overall framework

In order to evaluate the universality of the control method in the target angle range, $1°, 90°, 180°, 270°$ are set as the target angle of the simulation. The evaluation indexes of the control method are angle positioning error, running time, armature current and control voltage, and the indexes are shown in table Tab. 5.

Tab. 5 Details of assessment indicators

Evaluation index	Sign	Implication	Dimension
control voltage	u_a	The real-time input voltage of the motor controlled according to Eq. (26)	V
motor running time	t_e	The time interval between motor start and stop	s
angle convergence time	t_s	Time interval between motor start-up and angle error convergence	s
angular positioning error	$\Delta\theta(t_e)$	When the rotation angle of the motor converges, the difference between the actual angle and the target angle.	°
armature current	i_a	The instantaneous armature current of the motor is calculated according to Eq. (18).	A

In order to ensure the fairness and consistency of the controller comparison, the maximum rotation angle

condition (360°) is used as the reference condition, and the parameters of the three controllers are uniformly tuned. The parameters of each controller are optimized by step response test under this condition, so that the system can obtain the best dynamic response characteristics. The parameters after tuning are shown in

Tab. 6.

Tab. 6 The tuning results of each controller parameter

Method	Setting parameter	Parameter value	$t_e/(s)$	$\Delta\theta(t_s)/(°)$	$t_s/(s)$
Method 1	$[\Theta_{\text{th}} \quad D]$	[80° 3.8]	2.76	0.0022	2.73
Method 2	$[K_P \quad K_I \quad K_D]$	[0.08 0.0109 0.01]	1.09	-0.0253	1.70
Method 3	$[K_P \quad K_I \quad K_D]$	[0.795 0.001 0.29]	4.78	0.0339	4.75

The control voltage and angle error comparison curves of the three methods at 360° target angle are shown in Fig. 10. It can be observed that the difference between the motor running time and the angle convergence time of Method 2 is 0.61 s, the angle positioning error is − 0.0253°, and the angle error of the motor is 0.0022° when t = 1.68 s. It can be seen that this method has a lag in the control of the motor rotation angle, resulting in the overshoot of the motor rotation angle. At 360°, the angle control requirements can be met by parameter adjustment, but switching another target angle will lead to an increase in the positioning error. It can be seen that the linear control method of Method 2 cannot solve this problem. The motor running time and angle convergence time of Method 1 and Method 3 are theoretically equal, that is, the rotation speed of the motor can be guaranteed to be 0 when the motor stops, which is suitable for the control problem in this paper. Therefore, the simulation comparison between method 1 and method 3 is carried out to reflect the superiority of the method proposed in this paper.

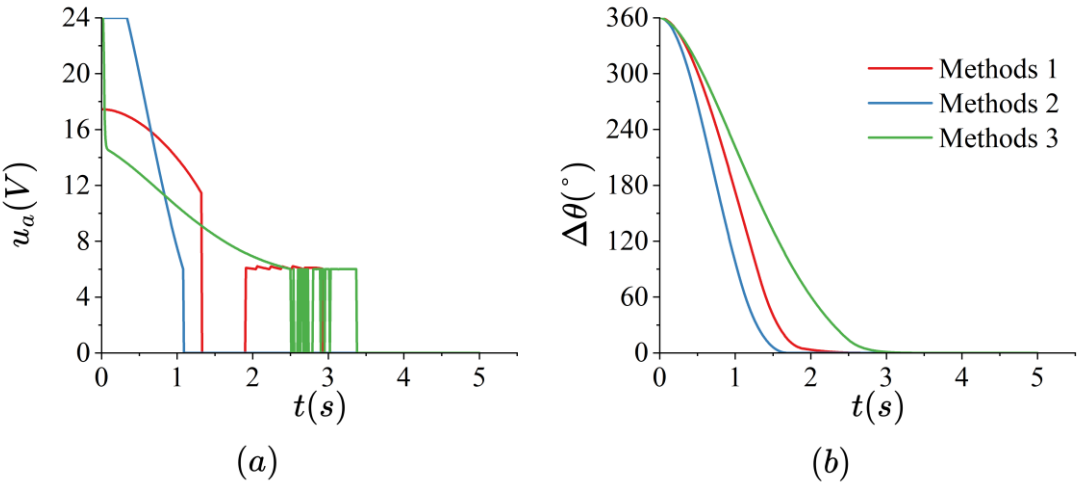


Fig. 10 $\Delta\theta = 360°$ control situation

4.3 Simulation results comparison

The steady-state positioning error and convergence time statistics of the two control methods at each target angle are as

Tab. 7, and the corresponding angle error time series curve is shown in Fig. 11.

Tab. 7 Control of each target angle

Method	Angle on target /(°)	$\Delta\theta(t_s)/(°)$	$t_s/(s)$
Method 1	1	0.0381	0.46
	90	0.0082	3.28
	180	0.0079	3.41
	270	0.0213	3.06
Method 3	1	0.0252	3.27
	90	0.6173	4.03
	180	-0.1339	5.25
	270	-0.0451	4.90

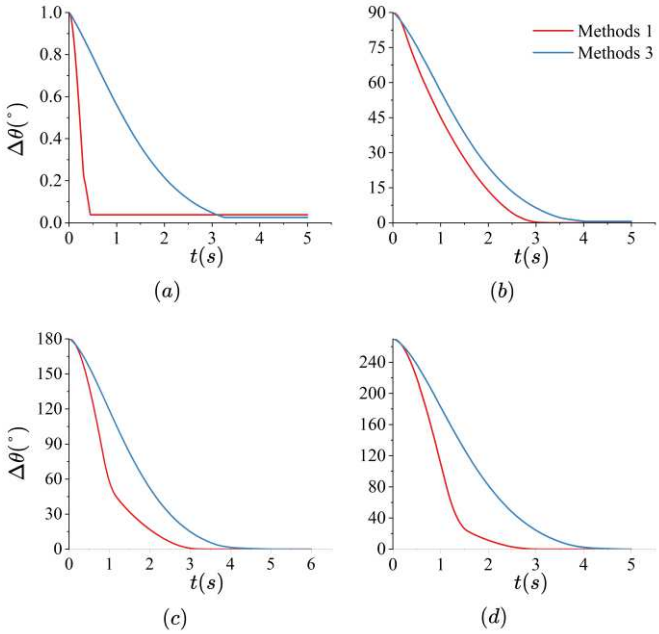


Fig. 11 Angle error timing

From the perspective of positioning accuracy, the error performance of this method in the full test angle range is stable and uniform. The maximum absolute positioning error under the four working conditions occurs at 1°, and the error is 0.0381°. Under the conditions of 90° and 180°, the error is less than 0.01°, and the accuracy is the best. The error is 0.0213° under 270° large angle condition, which is still maintained at a high accuracy level. On the whole, the error amplitude does not show a systematic offset with the total travel of the target angle, and the fluctuation range of the whole interval error is 0.0302°, which has a strong target angle independence. This is because the velocity constraint of the position loop is completely determined by the current residual angle and the physical parameters of the system, and is not directly related to the total amplitude of the target angle.

In contrast, the positioning accuracy of method 3 shows a strong condition dependence. At a large angle of 270° close to the setting condition (360°), the absolute positioning error is 0.0451°, which is in the same order of magnitude as the method in this paper. However, when the target angle deviates from the setting interval, the control accuracy is significantly degraded. For example, the absolute error is as high as 0.6173° at 90°, which is 75 times that of the method in this paper. This is because the cascade PID control law is constructed based on the time domain error integral, and the output and the remaining stroke lack the corresponding relationship at the physical level. The damping and gain parameters set under the 360° condition are applied to

the small and medium angle conditions. The braking time and deceleration rate of the system do not match the actual stroke, which eventually leads to a large drift of the positioning error.

From the perspective of convergence efficiency, the response speed of the proposed method in the whole angle range is significantly better than that of method 3, and the advantage becomes more prominent with the decrease of the target angle. Under the condition of 1° small angle, the method in this paper only needs 0.46s to complete the positioning, while the cascade PID needs 3.27s, and the response speed is increased by about 6 times. Under medium and large angle conditions, the convergence time of the proposed method is controlled within 3.41s, and the convergence time under 180° condition is about 35% shorter than that of cascade PID. The speed planning of the method in this paper takes the energy dissipation limit as the boundary, and runs at the maximum safe speed under the current residual angle. The initial response of the response process is rapid, the end is convergent and crisp, and there is no low-speed creeping phenomenon. In Method 3, when the angle is close to the target value, the cumulative output of the integral term cannot be quickly subsided, and the system creeps to the target at a very low speed for a long time, which greatly prolongs the overall convergence time.

The control voltage and current comparison curves of the two methods are shown in Fig. 12-13. In the stage of start-up and uniform operation, the mapping relationship between voltage output and target speed is clear, and the waveform is stable as a whole. However, in the interval where the residual angle is close to the dead zone threshold at the end of braking, the control voltage has a slight jump phenomenon. The jump phenomenon of the control voltage effectively avoids the motor entering the low-speed creep state and accelerates the convergence speed of the later operation angle. In contrast, the control voltage of method 3 is smooth and continuous without obvious fluctuation, which makes the voltage unable to decay rapidly with the remaining angle, and a long time small voltage tailing occurs at the end, which prolongs the convergence time of the system. The overall trend of current and voltage is consistent, but the current amplitude of method 3 is too large, reaching a maximum of 0.7191A, but both are within the maximum current range of the motor.

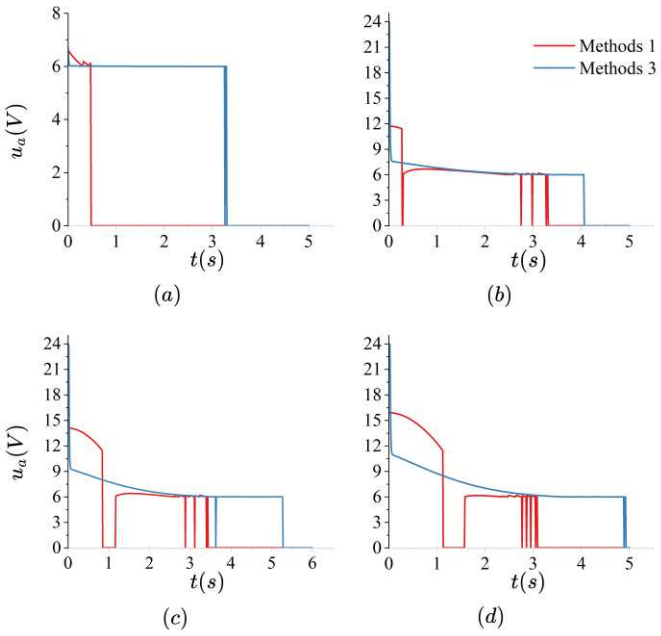


Fig. 12 Voltage command timing

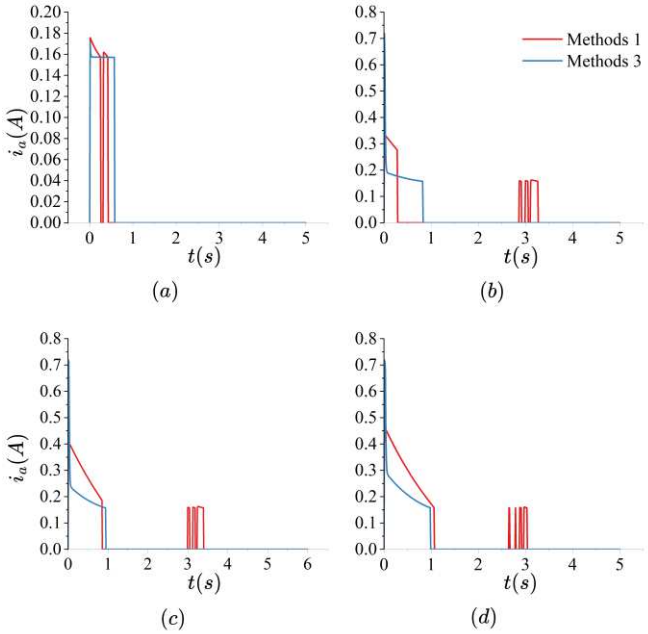


Fig. 13 Current comparison curve

Through comprehensive analysis, the performance difference between the two control methods is due to the essential difference of the control architecture. The advantages of this method mainly include the following three points.

(1). The method in this paper belongs to position domain control. The control law is directly driven by the residual angle, and the output is strictly corresponding to the physical stroke, which is naturally independent of the target amplitude. Method 3 belongs to the time domain control, and the output is determined by the time accumulation of the error. The change of the target stroke will directly affect the accumulation amount, so the performance is easy to drift with the working condition.

(2). The method in this paper is based on the physical parameters of the motor and the mechanism, which belongs to model-driven control, and the control logic is deeply adapted to the physical constraints of the system. Method 3 belongs to data-driven feedback control, which does not depend on the system model, but the parameter setting is highly dependent on the working condition, and the generalization ability is limited.

(3). Starting from the energy constraint, the method in this paper guarantees the non-overshoot characteristic from the mechanism, and fully adapts to the hard constraint of unidirectional rotation. Method 3 needs to avoid overshoot through conservative tuning, which inevitably sacrifices the response speed, and cannot meet the requirements of no overshoot and rapidity in the full angle range.

For the controlled object such as the eccentric ring of the rotary steering tool with one-way rotation hard constraints and the need for full-stroke general control, the method proposed in this paper has significant comprehensive advantages in positioning accuracy, response efficiency and parameter universality, and can better meet the needs of practical engineering applications.

5 Experimental verification

5.1 Construction of test prototype platform

In order to verify the actual control performance and engineering feasibility of the proposed control algorithm, a test prototype platform of double eccentric ring guiding mechanism is built in this paper. The

platform consists of three parts: mechanical actuator, hardware measurement and control circuit and host computer monitoring system. It can realize closed-loop control of eccentric ring angle, multi-parameter real-time acquisition and online verification of control algorithm. The test prototype adopts the static bias pointing double eccentric ring structure as the execution body, and the physical structure is shown in Fig. 14. The mechanism mainly includes inner and outer eccentric ring drive motor, eccentric ring assembly, ratchet bearing, gear transmission pair and Hall position detection unit. The overall width of the prototype is 60 cm and the axial length is 70 cm. It can simulate the motion characteristics of the eccentric ring under downhole conditions and provide a reliable mechanical carrier for the verification of the control algorithm.



Fig. 14 Eccentric ring prototype physical map

The measurement and control circuit takes the GD32 F103 RCT6 microcontroller as the core, and uses Altium Designer to complete the schematic and PCB design. The hardware design and verification results are shown in Fig. 15-17. The circuit board is divided into four modules according to the function, the left side is a 24V DC input and power conversion circuit, which can output stable 5 V and 3.3 V voltages to supply power to each module; the middle area is GD32 main control chip and peripheral circuit, which is responsible for running control algorithm, generating PWM drive signal and processing sensor feedback data. The right side is the motor drive and current detection circuit to realize the motor speed regulation and running current acquisition. The attitude detection circuit is integrated on the back of the circuit board, which can obtain the attitude Euler angle of the tool in real time. The DC scanning simulation results of the power supply circuit are shown in Fig.16. The output voltage stability of 3.3V and 5V is good, and there is no obvious ripple and voltage drop, which meets the power supply requirements of the system. The final physical circuit board size is 21cm × 5cm, high integration, can adapt to the narrow installation space.



Fig. 15 Eccentric ring hardware system PCB



Fig. 16 Eccentric ring hardware system power supply simulation



Fig. 17 Eccentric ring control hardware circuit board

The upper computer operation interface of the system is shown in Fig. 18. The motion control module supports two modes of manual control and automatic control. The operator can issue the target angle instructions of the inner and outer eccentric rings, and realize two-way data interaction with the lower computer through the serial port, which is convenient for parameter debugging and control effect observation during the test.



Fig. 18 System host computer control software

5.2 Test result analysis

In order to verify the control accuracy, dynamic characteristics and operational reliability of the control algorithm in the actual physical system, a closed-loop control verification experiment was carried out on the

above-mentioned double eccentric ring test prototype platform. In the experiment, the target angle command is issued by the upper computer, and the lower computer runs the control algorithm independently and completes the full closed-loop position adjustment. The angle and temperature state data are collected synchronously, and the engineering applicability of the algorithm is evaluated from the steady-state positioning accuracy and thermal stability.

In the experiment, 10 groups of typical target angle combinations are selected, covering various working conditions such as single-loop independent motion and double-loop linkage. The actual arrival angles of the inner and outer eccentric rings in each group of experiments are recorded, and the control accuracy is calculated by relative deviation. The test results are shown in Tab. 8.

The results show that the control errors of the inner and outer eccentric rings are less than 0.8° under the full test conditions. The maximum absolute positioning error of the inner eccentric ring is 0.8° (corresponding to the target angle of 30°), and the maximum absolute positioning error of the outer eccentric ring is 0.6° (corresponding to the target angle of 72°). The positioning error of the system mainly comes from the mechanical clearance of the gear transmission pair, the resolution limit of the Hall position sensor and the assembly coaxiality deviation. The overall error level meets the requirements of the wellbore trajectory control accuracy of the rotary steering tool. Under the condition of double-loop synchronous linkage, there is no significant attenuation of the control accuracy of the two loops, which shows that the proposed method has good suppression ability for multi-axis coupling disturbance, and the robustness of the algorithm is in line with the expectation of engineering application.

Tab. 8 Internal and external eccentric ring control precision test table

measurement times	Setting angle of inner eccentric ring /°	Setting angle of the outer eccentric ring /°	Measured angle of inner eccentric ring /°	Measured angle of outer eccentric /°	Control error of inner eccentric ring /°	Control error of outer eccentric ring/°
1	30	0	30.8	0	0.8	0
2	60	0	59.9	0	0.1	0
3	0	36	0	35.5	0	0.5
4	0	72	0	71.6	0	0.6
5	30	36	29.9	36.2	0.1	0.2
6	60	72	60.3	71.8	0.3	0.2
7	90	108	89.4	108.1	0.6	0.1
8	180	216	179.7	216.5	0.3	0.5
9	270	324	269.5	324.2	0.5	0.2
10	300	360	298.8	359.6	0.2	0.4

In order to evaluate the thermal stability of the continuous operation of the system, the temperature of the tool body of 10 continuous positioning experiments was collected synchronously, and the temperature change

trend was shown in Fig. 19.

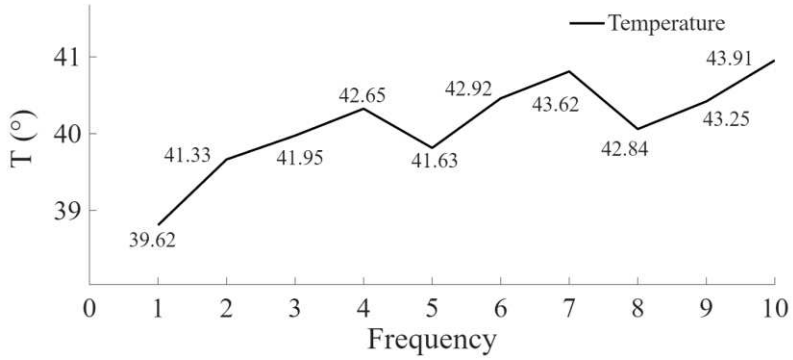


Fig. 19 Intelligent control experimental tool temperature line chart

According to the temperature curve, the temperature of the tool body increases slowly with the increase of the number of runs, and finally tends to be stable. The maximum temperature of the whole process is 43.91°C. The temperature is far lower than the conventional rated working temperature threshold of the downhole measurement and control device, which meets the engineering requirements.

In summary, the experimental results verify the engineering effectiveness of the control scheme proposed in this paper. The system has high positioning accuracy and gentle temperature rise, and the overall performance meets the application requirements of the rotary steering tool.

6 Conclusion

In this paper, a three-stage closed-loop control method of velocity planning based on the principle of energy conservation is proposed for the high-precision angle servo control problem of the double eccentric ring mechanism of the static bias pointing rotary steering tool under the unidirectional rotation constraint. The hierarchical control architecture of position-velocity-voltage is formed, and the effectiveness and engineering applicability of the method are verified by simulation and experimental systems.

Based on the principle of energy conservation, the position loop proposed in this paper calculates the maximum safe speed under the constraint of residual angle in real time to ensure that the system brakes at the target position after removing the driving force, which naturally eliminates the possibility of overshoot. In the speed loop, the back electromotive force feedforward mapping is used to replace the traditional PI error accumulation to avoid integral saturation and phase lag. The voltage loop ensures the safe operation of the actuator through saturation limiting and dead zone management. The three-level loop function decoupling is clear, the physical meaning is clear, and the parameter adjustment logic is independent.

Through simulation analysis, compared with traditional PID and cascade PID control, this method maintains stable positioning accuracy in the full target angle range (1° -360°), and the maximum absolute error is 0.0381°, while the cascade PID deviates from the setting condition. The error is as high as 0.6173°. In terms of convergence efficiency, the proposed method only takes 0.46s under the condition of 1° small angle, which is 6 times higher than that of cascade PID. The terminal hopping strategy of the control voltage effectively avoids low-speed creep and improves the convergence speed.

In order to verify the feasibility of the method, the positioning error of the double eccentric ring experimental prototype based on GD32 microcontroller is less than 0.8° under 10 groups of typical target angle conditions, which meets the basic requirements of the guidance function of the rotary guidance tool. The

temperature of the tool body is up to 43.89°C after continuous operation, which is far lower than the rated working threshold of the downhole measurement and control device, and the system has good thermal stability.

The proposed method reveals the control essence of non-overshoot positioning under unidirectional rotation constraints. The speed boundary is defined by the energy dissipation limit, and the constraint satisfaction is transformed from the parameter passive tuning problem to the physical-driven active planning problem. The practical significance is to provide a full-stroke universal, parameter physicalization, and simple engineering implementation solution for the eccentric ring angle servo of the rotary steering tool.

The future research work will focus on the following directions: First, an adaptive resistance torque observer is introduced to identify friction and load changes online to further improve the anti-disturbance ability ; second, further experimental verification is carried out under actual downhole conditions to lay a more solid foundation for engineering applications.

Reference：

[1] Feng, D., Wang, P., Zhang, H., et al. Research status and development trend of rotary steerable tools[J]. China Petroleum Machinery, 2021, 49(7): 8-15.DOI:10.16082/j.cnki.issn.1001-4578.2021.07.002.

[2] Wang H, Guan Z C, Shi Y C, et al. Study on build-up rate of push-the-bit rotary steerable bottom hole assembly[J]. Journal of applied science and engineering, 2017, 20(3): 401-408.

[3] Abdulgalil F, Siguerdidjane H. PID based on sliding mode control for rotary drilling system[C]//EUROCON 2005-The International Conference on" Computer as a Tool". IEEE, 2005, 1: 262-265.

[4] Liu Qingbo, Di QingYun, Wang XiangYang, et al. Measurement and control system of the stabilized-platform rotary steerable system[J]. Chinese Journal of Geophysics, 2025, 68(06): 2416-2431.

[5] Li S, Wang Y, Wu X, et al. Self-stabilizing control strategy of stabilized platform for rotary steerable drilling system based on adaptive backstepping control[C]//Actuators. MDPI, 2024, 13(3): 116.

[6] Li S, Wang Y, Wang D, et al. Backstepping sliding mode control of stabilized platform for fully rotary steerable drilling system based on nonlinear disturbance observer[J]. Energy Science & Engineering, 2024, 12(4): 1775-1791.

[7] Liang Y, Kang H, Liu Y, et al. Design and Implementation of Closed-Loop Control of Vector Force in Static Push-the-bit Rotary Steering System[J]. Applied Geophysics, 2025, 22(3): 796-803.

[8] Gao M, Cheng W, Wei Y, et al. Adaptive fixed-time fault-tolerant tracking control for rotary steerable drilling tool systems[J]. Control Engineering Practice, 2024, 150: 106004.

[9] Zhang K, Huo A. Deep reinforcement learning attitude control of stabilized platform for rotary steerable system based on extended state observer[J]. Journal of Engineering Research, 2024.

[10] Zhang N, Li F, Liu Z, et al. Inclination-holding Control Method for Rotary Steerable System Based on Fuzzy-PID[C]//2024 6th International Conference on Intelligent Control, Measurement and Signal Processing (ICMSP). IEEE, 2024: 31-34.

[11] Huo A, He Y, Wang Y, et al. Research of disc valve friction torque modeling and integral sliding mode adaptive control for rotary steering drilling tool[C]//2010 2nd International Conference on Computer Engineering and Technology. IEEE, 2010, 1: V1-715-V1-719.

[12] Gan, D. R. Application of low-pass filter in control system of rotary steerable drilling tool[J]. Information Recording Materials, 2019, 20(9): 117-119.

[13] Zhang, G. W., Gao, X., & Gan, D. R. Research on double-loop integral sliding-mode control for downhole closed-loop steerable drilling tool[J]. Journal of Xi'an Shiyou University (Natural Science Edition), 2019, 34(3): 69-73, 80.

[14] Cao, X. J. Research on intelligent control system of eccentric-ring for rotary steerable drilling tool[D]. Yangtze University, 2023.

Funding

This work was supported by the National Natural Science Foundation of China (Grant No. 52204002).